AGU PUBLICATIONS

Radio Science

RESEARCH ARTICLE
10.1002/2015RS005889

Special Section:
Ionospheric Effects Symposium 2015

Three-dimensional modeling of high-latitude scintillation observations

Alex Chartier[1], Biagio Forte[2], Kshitija Deshpande[3], Gary Bust[1], and Cathryn Mitchell[2]

[1]The Johns Hopkins University Applied Physics Laboratory, Laurel, Maryland, USA, [2]Department Electronic and Electrical Engineering, University of Bath, Bath, UK, [3]Bradley Department of Electrical and Computer Engineering, Virginia Polytechnic Institute and State University, Blacksburg, Virginia, USA

Key Points:
- High-latitude E region irregularities modeled with 3-D multiple phase screens
- Model ingests EISCAT electron density observations
- Model results provide a reasonable match to GPS observations

Correspondence to:
A. Chartier,
alex.chartier@jhuapl.edu

Citation:
Chartier, A., B. Forte, K. Deshpande, G. Bust, and C. Mitchell (2016), Three-dimensional modeling of high-latitude scintillation observations, *Radio Sci.*, *51*, 1022–1029, doi:10.1002/2015RS005889.

Received 30 NOV 2015
Accepted 24 JUN 2016
Accepted article online 30 JUN 2016
Published online 15 JUL 2016

Abstract Global Navigation Satellite System signals exhibit rapid fluctuations at high and low latitudes as a consequence of propagation through drifting ionospheric irregularities. We focus on the high-latitude scintillation problem, taking advantage of a conjunction of European Incoherent Scatter Radar (EISCAT) observations and a GPS scintillation monitor viewing the same line of sight. Just after 20:00 UT on 17 October 2013, an auroral *E* region ionization enhancement occurred with associated phase scintillations. This investigation uses the scintillation observations to estimate the ionospheric electron density distribution beyond the spatial resolution of EISCAT (5–15 km along the line of sight in this case). Following the approach of Deshpande et al. (2014), signal propagation is modeled through a specified density distribution. A multiple phase screen propagation algorithm is applied to irregularities conforming to the description of Costa and Kelley (1977) and constrained to match the macroscopic conditions observed by EISCAT. A 50-member ensemble of modeled outputs is approximately consistent with the observations according to the standard deviation of the phase (σ_p). The observations have $\sigma_p = 0.23$ rad, while the ensemble of modeled realizations has $\sigma_p = 0.23 + 0.04–0.04$. By comparison of the model output with the scintillation observations, we show that the density fluctuations cannot be a constant fraction of the mean density. The model indicates that *E* region density fluctuations whose standard deviation varies temporally between 5 and 25% of the mean (EISCAT-observed) density are required to explain the observed phase scintillations.

1. Introduction

Scintillation is the phenomenon of random phase and intensity fluctuations in received radio signals. Scintillation is seen in transionospheric signals in the frequency range of 100 MHz to 4 GHz [*Basu et al.*, 1988; *Aarons and Basu*, 1994]. At high latitudes, scintillation caused by *E* region auroral events can be strong enough to cause loss of lock by GPS L-band receivers [*Skone and De Jong*, 2000; *Smith et al.*, 2008]. Physically, scintillation is caused by diffractive scattering and refractive lensing of signals by ionospheric electron density structures. At GPS frequencies (L1: 1575 MHz, L2: 1228 MHz), intermediate-scale irregularities (approximately 0.1–10 km) are responsible for diffractive scattering.

1.1. Signal Propagation

At high latitudes, phase scintillation is frequently observed without accompanying intensity scintillation [*Aarons*, 1997; *Skone et al.*, 2008; *Azeem et al.*, 2013]. The phenomenon has been addressed theoretically by *Booker et al.* [1950], *Rino* [1979], *Yeh and Liu* [1982], *Kintner et al.* [2007], and others. Signal phase and intensity can behave differently because they respond to different irregularity scale sizes. The Fresnel radius defines the most effective irregularity scale for intensity scintillation. The Fresnel radius is ~270 m for L1 signals when the irregularity layer is at a range of 150 km from the receiver. In principle, the signal phase responds to irregularities of all scale sizes. In practice, however, an artificial outer scale is imposed beyond which electron density variations have practically no effect [*Forte and Radicella*, 2004]. This outer scale occurs because observational data are detrended to remove long-period fluctuations. In the case of a 0.1 Hz filter and a 300 m/s effective velocity there is an artificial outer scale of 3000 m for the phase.

1.2. Auroral Scintillation

Evidence of scintillation on L-band GPS signals in conjunction with auroral structures has been provided by *Skone et al.* [2001], *Prikryl et al.* [2011], and *Kinrade et al.* [2013]. Currently, there are no *E* region electron

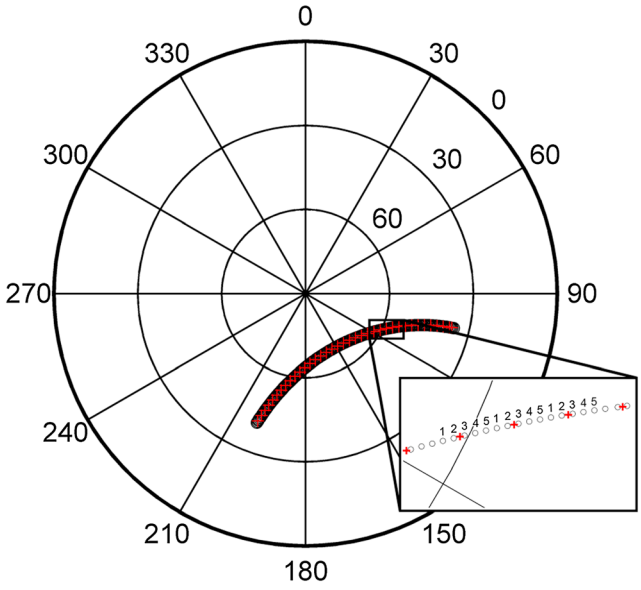

Figure 1. The azimuth and elevation of the EISCAT beam during the scintillation experiment. The beam moves every 5 min, stopping at the central location of the GPS satellite for that period.

density observations of sufficiently high spatial resolution to determine the irregularity distributions responsible for these scintillations.

The aim of this investigation is to determine the irregularity distribution characteristics using a constrained modeling approach to match the scintillation observations. Despite the unprecedented conjunction of data available in this case, some model parameters remain unconstrained by observations. These are the effective irregularity drift velocity, the fractional density fluctuation ($\Delta N/N$), and the axial ratio of the irregularities. Choices of these parameters are informed by the parameter space search performed by *Deshpande et al.* [2014], by prior observational studies and by the observed scintillation signal.

2. Observations

The present study is based on an experiment where the European Incoherent Scatter Radar (EISCAT) is operated along the line of sight of GPS satellites, by tracking their motion across the sky. In the selected case study phase scintillation is observed at Tromsø, Norway, just after 20:00 UT on 17 October 2013. The K_p index of 1^+ between 18:00 and 21:00 UT indicates quiet geomagnetic conditions during the experiment. Similar scintillation cases are not especially rare in themselves, but we are not aware of another case with direct supporting observations from EISCAT along the GPS line of sight.

The EISCAT UHF antenna tracked the location of GPS satellite PRN 23, making ionospheric electron density observations along the line of sight using the calibrated backscattered power from its 931 MHz transmissions. The dish changed position every 5 min, with the satellite moving across it in that period. Five 60 s integrations are made at each location, from which electron density, ion and electron temperature, and beam-parallel ion drifts can be calculated. This EISCAT experiment was monostatic, so no estimate of cross-track drifts can be made. At the time of interest (~20:05 UT), the angle between the beam and the magnetic field is around 25°. The azimuth and elevation of the beam are shown in Figure 1.

A collocated Novatel GSV4004 GPS ionospheric scintillation monitor receives transmissions from the same satellite (PRN 23). The scintillation monitor outputs scintillation indices, TEC and TEC rate of change at 1 min intervals, together with 50 Hz signal intensity and phase [*Van Dierendonck et al.*, 1993]. The 50 Hz intensity and phase are used for this study.

EISCAT electron densities and GPS scintillation observations are shown in Figure 2. Scintillation data are detrended using a third-order polynomial followed by a sixth-order 0.1 Hz high-pass Butterworth filter. At 20:05:20 UT, a phase scintillation spike of over 3 rad peak to peak is observed that corresponds with enhanced *E* region electron densities that peak at 4.17×10^{11} el/m^3 at 132 km. Smaller phase scintillations occur from 20:04:30 to 20:07:00 UT. No corresponding spike in the observed signal intensity is observed above the noise floor.

Power spectral densities are calculated on the unfiltered signal phase and intensity during the same period to determine the characteristics of the ionospheric irregularities responsible for the scintillation. The region $>$0.1 Hz is directly comparable with the filtered signal of Figure 2. Welch's power spectral density method is used with a Hamming window, eight segments, and a 50% overlap. The time interval considered is

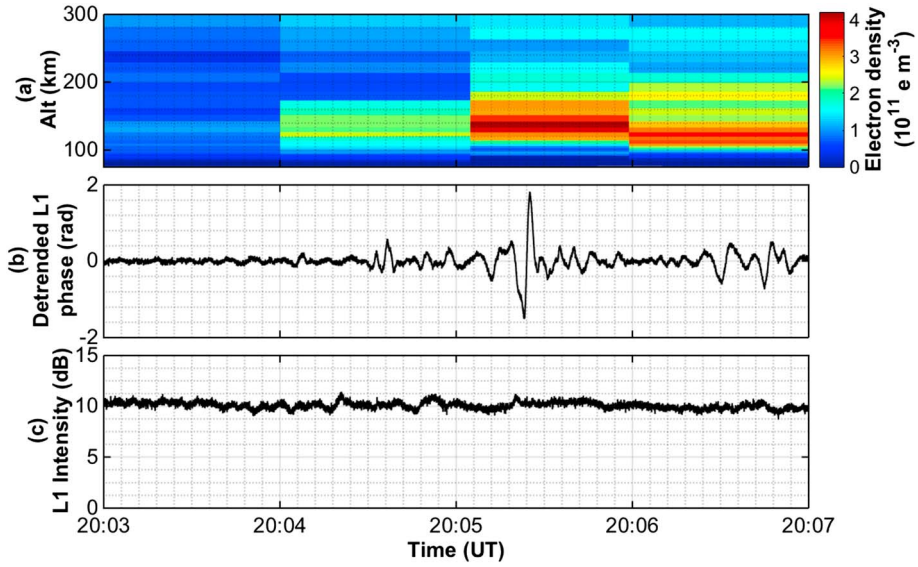

Figure 2. (a) EISCAT electron densities, (b) 50 Hz detrended GPS L1 carrier phase, and (c) 50 Hz signal intensity.

20:03 to 20:07 UT. These spectra are shown in Figure 3. The signal phase has a clear linear slope of −4.2 down to a noise floor above 1 Hz. The signal power does not have a single clear slope, although an increase above the noise floor is evident at lower frequencies.

3. Modeling

Given the supporting information available from EISCAT, it is possible to model GPS signal propagation through the ionosphere in this case. The comparison between modeled and observed results is used to understand what combination of parameters drives this particular event. The SIGMA scintillation model developed by *Deshpande et al*. [2014] is used here. SIGMA is a three-dimensional, multiple phase screen scintillation model that accounts for satellite and irregularity motion and allows for anisotropic irregularity modeling. For this study, EISCAT electron density data are ingested to specify the macroscale ionospheric electron densities. The geometry of the electron density representation is modified from the approach of *Deshpande et al*. [2014], but the signal propagation algorithm and the irregularity spectrum generator (based on the formulation of *Costa and Kelley* [1977]) remain unchanged. The spectrum $\boldsymbol{P}$, shown in equation (1), depicts a Gaussian density distribution along the magnetic field direction k_z and a power law variation perpendicular to it (in the plane of k_x and k_y):

$$\boldsymbol{P}(\boldsymbol{k}) = \frac{a\ \ \gamma\ \ \sin(3\pi/\gamma)}{4\pi^2 {k_0}^3}\Delta N^2 \cdot \left\{ \left(1 + \frac{k_x^2 + k_y^2 + a^2 k_z^2}{{k_0}^2} \right)^{-\gamma/2} \right\}^{-1} \tag{1}$$

Here $\boldsymbol{k} = (k_x, k_y, k_z)$ is the spatial wave number vector, γ is the spectral index, a is the axial ratio, ΔN is the root-mean-square density fluctuation, and k_0 is the wave number associated with the outer scale of the irregularity spectrum.

3.1. Electron Density Representation

A geometry change is introduced to SIGMA for this study in order to drastically reduce computation times. Instead of using a static horizontal/vertical grid large enough to capture all raypaths throughout the experiment, we align our grid along the satellite-receiver line of sight at each time step (see Figure 4). The result is that the representation volume must only extend a few Fresnel radii in the perpendicular directions to capture weak scatter effects, and so computation times are reduced down to faster than real time for short (5 min) simulation periods (depending on resolution). This approximation is valid only in weak scatter cases, such as the case addressed here. A larger perpendicular extent would be required to capture the effects of strong scatter.

To understand the scintillation that results from signal propagation through a given ionospheric irregularity distribution, the altitude and thickness of the irregularity layer and the apparent velocity perpendicular to the

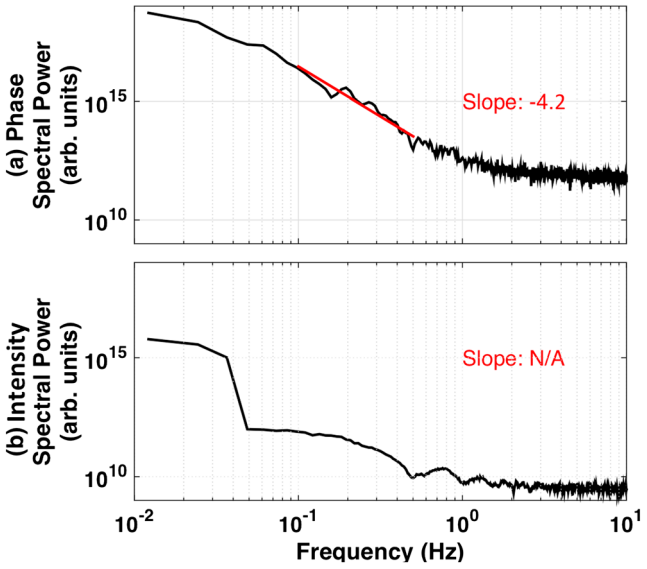

Figure 3. Power spectral density of (a) GPS signal phase and (b) signal intensity. A linear fit of −4.2 is achieved to the phase spectrum unaffected by noise (defined as between 0.1 and 0.5 Hz). No linear slope can be identified in the intensity.

line of sight must be known. We do not have direct observations of these parameters, so it is necessary to make some assumptions. Given the electron density enhancements observed by EISCAT and shown in Figure 2, we assume that associated irregularities are formed in the region ~95–175 km altitude (110–200 km range). The gradients associated with the irregularities (ΔN) are assumed to be a varying proportion of the background density, so that the mean-squared fractional fluctuation density $\overline{\left(\frac{\Delta N}{N}\right)^2}$ is allowed to vary in time. In this case EISCAT is operated in monostatic mode and so observes only the component of bulk plasma velocity in a single line of sight between the GPS satellite and receiver, so it is not possible to deduce the effective drift velocity of the irregularities. A velocity of 300 m/s is found to be the lowest that produces an accurate match to both the phase and intensity spectra shown in Figure 3. This is below the ion acoustic velocity (~500 m/s at 150 km altitude increasing to ~1000 m/s at 220 km, using EISCAT temperatures and assuming ion molar mass of 28) and well within the normal range of ion drift velocities seen at auroral latitudes, which can be as high as 1000 m/s or more [e.g., *Chisham et al.*, 2007]. The slope of the power spectral density is set to −4.2, and there is effectively no outer scale (lengths beyond 3 km are removed by the 0.1 Hz high-pass filter). The axial ratio is set to 1 in this case. This is necessary because, in this case, values larger than 1 cause the modeled intensity fluctuations to rise above what is observed. It is worth noting that this value is much lower than what *Gola et al.* [1992] found to fit most auroral cases (values between 6 and 15), so this event may be seen as unusual.

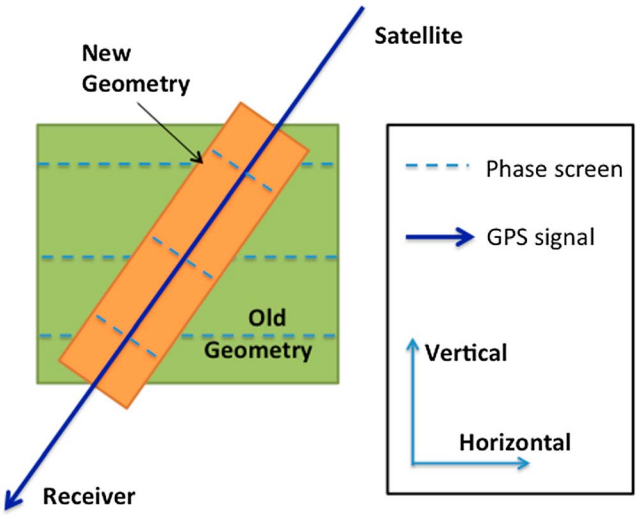

Figure 4. The geometry change introduced to SIGMA for this study. The new geometry (orange) allows for smaller phase screens and thus faster computation times and lower memory requirements.

It is not possible to match the time domain phase signal (Figure 2) with $\overline{\left(\frac{\Delta N}{N}\right)^2}$ set to a constant, so it is necessary to vary ΔN between 5 and 25% of N. Even with this, the large (>3 rad) spike observed at 20:05:25 cannot be reproduced, so a kilometer-scale enhancement is added to the irregularity spectrum at that time. This transient spike has no appreciable effect on the modeled spectra. The resulting modeled electron density distribution is shown in Figure 5.

The electron density representation shown in Figure 5 is moved along the Y direction, across the direction of signal propagation (Z), at an effective drift velocity of 300 m/s. This is the lowest velocity that could be used that matched the observed

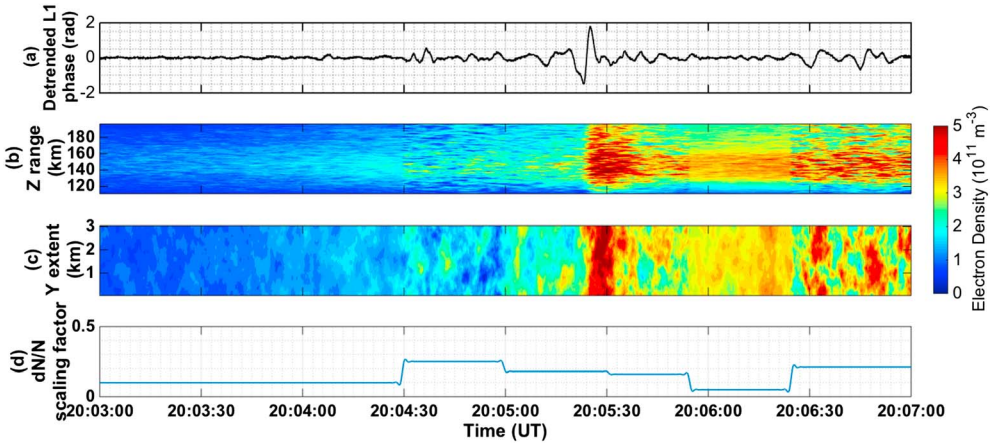

Figure 5. (a) The observed detrended phase is repeated from Figure 2; (b) range-time profile of an example model electron density configuration, based on EISCAT observations of the background density with one realization of Costa-Kelley irregularities added; (c) cross-track profile of the same model densities; and (d) the variable irregularity scaling factor. Three phase screens are constructed perpendicular to *Z* (at 125, 155, and 185 km) from this density distribution.

phase scintillation without changing parameters that would enhance the modeled signal intensity above what was observed. A sliding box is applied so that the *X* extent is always 3000 m (equivalent to 0.1 Hz at 300 m/s effective drift velocity), the same as the *Y* extent. A larger *X*/*Y* extent would have no effect on the result because a 0.1 Hz high-pass filter is applied to the results (described below).

3.2. Signal Propagation

The signal propagation algorithm developed by *Deshpande et al.* [2014] remains unchanged here. This is a modified version of *Rino*'s [1979] algorithm, so the electron density distribution in a layer is used to calculate a phase screen that is applied to the signal. Following *Knepp* [1983], multiple phase screens (three in this case) are used so that rescattering of the signal can be modeled. This is potentially an important feature at high latitudes where the irregularity region can extend for tens of kilometers or more due to the near-vertical orientation of the magnetic field.

The model configuration used for these simulations is set out in Table 1.

Fifty realizations of the model are produced using this configuration with different random number seeds for the irregularities. Figure 6 shows that the model reproduces the major features of the observed phase scintillation pattern in the time domain. Low-level (<0.25 rad peak-to-peak) phase fluctuations are observed before 20:04:30. Fluctuations increase to a moderate level (~1 rad peak-to-peak) between 20:04:30 and 20:05:55, with a large (>3 rad peak-to-peak) spike at about 20:05:25. There is a second low-level phase between 20:05:55 and 20:06:20, followed by a slightly more intense period (~1.5 rad peak-to-peak) thereafter. Both the modeled and the observed intensity fluctuations are small at all times. Slight enhancements seen in the modeled intensity fluctuations appear to be within the receiver noise of the observed intensity fluctuations (model values are shifted up 1 dB, so they can be seen clearly).

Table 1. Model Configuration

Parameter	Value
Sample frequency	10 Hz
Effective drift velocity	300 m/s
High-pass filter cutoff	0.1 Hz
Outer scale	3000 m (effectively none)
Axial ratio	1
Spectral index	4.2
Phase screens	3 (at 125, 155, and 185 km range)
Resolution (*X*, *Y*, *Z*)	30, 30, 100 m
Grid size (*X*, *Y*, *Z*)	3000, 3000, 90 000 m

The standard deviation is used to provide a quantitative performance metric here. This is calculated as shown in equation (2):

$$\sigma_p = \sqrt{\langle \phi^2 \rangle - \langle \phi \rangle^2} \qquad (2)$$

where ϕ is the detrended L1 carrier phase in radians and means are calculated over the time series shown in Figure 6. The observations have $\sigma_p = 0.23$ rad, while the ensemble of modeled realizations has

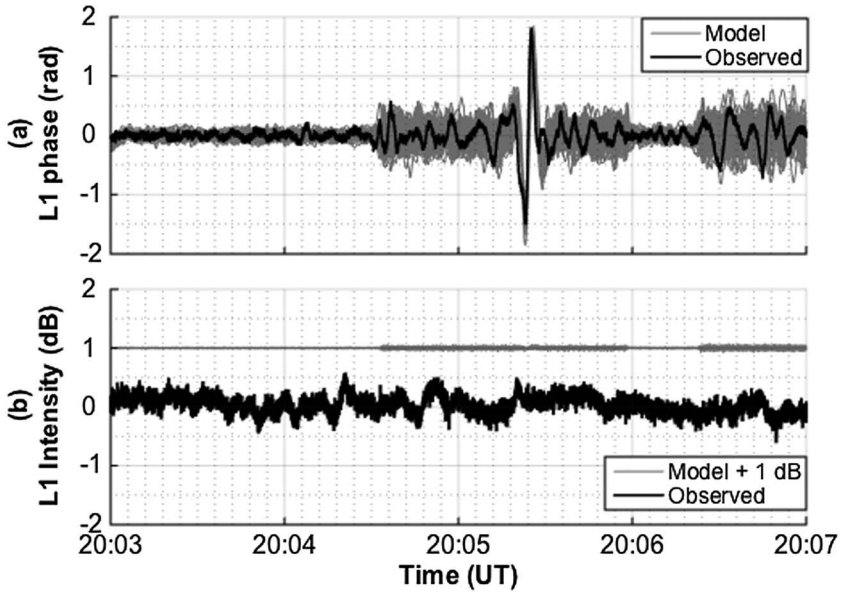

Figure 6. (a) The modeled (50 realizations in grey) and observed (bold black) detrended L1 carrier phase and (b) the L1 intensity. The modeled intensity is shifted up 1 dB so that it can be seen clearly.

$\sigma_p = 0.23 + 0.04–0.04$ rad (using mean, maximum, and minimum model values). It is worth noting that a single phase screen approach captures less scattering than the multiple phase screen approach in this case. The same model configuration as used above, except with a single screen at 155 km, produces lower $\sigma_p = 0.19 + 0.03–0.04$ rad.

The power spectral density (PSD) of the modeled phase and intensity are compared against the observations in Figure 7. The results are directly comparable in the range 10^{-1}–10^{0} Hz, where the signals are both above the noise floor and below the artificial 3000 m (equivalent to 0.1 Hz at 300 m/s effective drift velocity) outer scale imposed on the model for reasons of computational efficiency. In that range, the modeled and observed phase signals are in agreement since the observations lie within the range of model realizations. The modeled and observed power are both extremely weak, and while there is not a uniform slope evident

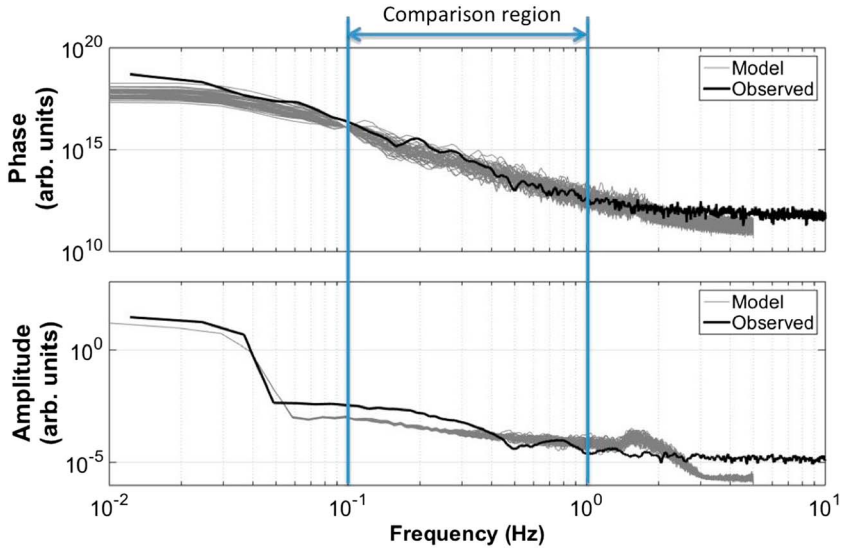

Figure 7. Power spectral densities of (top) phase and (bottom) intensity from the observations and 50 realizations of the model between 20:03 and 20:07 UT. Model values are normalized at 0.1 Hz.

in the observations, the two data sets can be considered approximately consistent. The observed intensity PSD has a similar shape at times outside of the phase scintillation event, so the two effects are likely unrelated.

4. Discussion

A new technique has been developed to ingest electron density observations into the SIGMA scintillation model. This development, combined with a geometry change that dramatically reduces computation times, allows for ensemble modeling of ionospheric scintillation. These developments have been used to compare model results against real scintillation observations in a specific auroral case study and to determine likely characteristics of the ionospheric irregularities responsible.

In this case, the model-observation comparison makes it possible to test the assumption that the mean-squared fractional density of ionospheric irregularities responsible for scintillation is a constant. Thanks to the availability of coaligned EISCAT and GPS data, it is possible to show that this assumption does not hold in this case. The magnitude of the phase scintillations is clearly not proportional to the background density as observed by EISCAT. In the model, the fraction $\frac{\Delta N}{N}$ has to be adjusted between 5 and 25% to achieve a match to the observations. A similar match could not have been achieved through adjustment of the other free parameters (effective drift velocity and axial ratio) within reasonable physical limits. This case may well be unusual since these irregularities are caused by an auroral *E* region enhancement rather than by *F* region convective processes. The unusual nature of this event is underlined by the steep slope of the phase PSD (-4.2).

It is possible to assess the performance of SIGMA in reproducing the observations if two limitations are taken into account. These are that an observational noise floor is evident above ~1 Hz and that the model is applied to scales $<$3000 m (frequencies higher than 0.1 Hz). Within the region where a direct comparison can be made (0.1–1 Hz), the results support the conclusion that the formulation of *Costa and Kelley* [1977] provides an accurate description of these irregularities and that our multiple phase screen signal propagation algorithm is suitable to characterize signal propagation in this case. It is worth noting that the transverse velocity of the irregularities (300 m/s) had to be estimated because of a lack of supporting observational evidence. The lowest suitable velocity was chosen here—a lower velocity would have required an increase in ΔN that would have caused more intensity scintillation than was observed. The axial ratio also had to be set to a rather unusual value of 1 in order to prevent any increase in the modeled intensity scintillation above what was observed.

The "frozen-in" assumption was used in the model results presented here. Since the model is broadly consistent with the observations, it appears that there is no need to invoke a more complicated, time-evolving irregularity distribution in this case. However, our results do not exclude the possibility that the irregularities evolve in time. The current modeling approach could be adapted to deal with time-evolving irregularities if cases are identified that cannot be represented otherwise.

The development of SIGMA for this study has greatly reduced computation times down to approximately real time for simulation periods of a few minutes (running in MATLAB on a laptop computer). This development permits the use of grids with *Z* extent large enough to simulate the effects of multiple scatter, which may be important for high-latitude scintillation. In this case we noted a discrepancy between the model using three phase screens and using just one. Assuming that the irregularity region truly extends for 90 km in the *Z* direction, as was specified here, this finding indicates that the effects of multiple scatter should be taken into account. While the observed density enhancement extends for 90 km, there is no proof that irregularities extend throughout that region. Therefore, we cannot exclude that a more intense but narrower region of irregularities exists.

5. Conclusions

The SIGMA model has reasonably accurately reproduced scintillations observed at Tromsø, which indicates that the modeled ionospheric irregularity distribution and signal propagation algorithm are likely to be consistent with the observations. A new grid geometry has been applied to the SIGMA model to achieve these results, with the positive consequence that computation times are greatly reduced. In this case, the results show that $\frac{\Delta N}{N}$ is not a constant, but the frozen-in assumption is consistent with the observations. Coupled with the steep slope of the phase PSD (-4.2) and axial ratio of 1, effective drift velocities of 300 m/s are sufficient to produce phase scintillation without having much effect on the modeled signal intensity, which is consistent with the observations.

Acknowledgments

We acknowledge the support of NSF grant AGS-1311922 in performing this work and NSF grant PLR-1243398 in developing the SIGMA model. The EISCAT experiment was led by PI Biagio Forte. Data can be retrieved from https://www.eiscat.se/madrigal/. Scintillation data were collected by PI Cathryn Mitchell on EPSRC grant EP/H003304/1 GNSS scintillation, detection, forecasting, and mitigation and can be obtained by contacting her.

References

Aarons, J. (1997), Global Positioning System phase fluctuations at auroral latitudes, *J. Geophys. Res.*, *102*, 17,219–17,231, doi:10.1029/97JA01118.

Aarons, J., and S. Basu (1994), Ionospheric amplitude and phase fluctuations at the GPS frequencies, in *Proceedings of the ION GPS-94*, pp. 1569, Inst. of Navigation, Arlington, Va.

Azeem, I., G. Crowley, A. Reynolds, J. Santana, and D. Hampton (2013), First results of phase scintillation from a longitudinal chain of ASTRA's SM-211 GPS TEC and scintillation receivers in Alaska, in *Proceedings of the ION PNT*, pp. 735–742, Inst. of Navigation, Arlington, Va.

Basu, S., E. MacKenzie, and S. Basu (1988), Ionospheric constraints on VHF = UHF communication links during solar maximum and minimum periods, *Radio Sci.*, *23*, 363–378, doi:10.1029/RS023i003p00363.

Booker, H. G., J. A. Ratcliffe, and D. H. Shinn (1950), Diffraction from an irregular screen with applications to ionospheric problems, *Philos. Trans. R. Soc. London A*, *242*(856), 579–607.

Chisham, G., et al. (2007), A decade of the Super Dual Auroral Radar Network (SuperDARN): Scientific achievements, new techniques and future directions, *Surv. Geophys.*, *28*(1), 33–109.

Costa, E., and M. C. Kelley (1977), Ionospheric scintillation calculations based on in situ irregularity spectra, *Radio Sci.*, *12*, 797–809, doi:10.1029/RS012i005p00797.

Deshpande, K. B., G. S. Bust, C. R. Clauer, C. L. Rino, and C. S. Carrano (2014), Satellite-beacon Ionospheric-scintillation Global Model of the upper Atmosphere (SIGMA). I: High-latitude sensitivity study of the model parameters, *J. Geophys. Res. Space Physics*, *119*, 4026–4043, doi:10.1002/2013JA019699.

Forte, B., and S. M. Radicella (2004), Geometrical control of scintillation indices: What happens for GPS satellites, *Radio Sci.*, *39*, RS5014, doi:10.1029/2002RS002852.

Gola, M., A. W. Wernik, S. J. Franke, C. H. Liu, and K. C. Yeh (1992), Behaviour of HILAT scintillation over Spitsbergen, *J. Atmos. Terr. Phys.*, *54*(9), 1207–1213.

Kinrade, J., C. N. Mitchell, N. D. Smith, Y. Ebihara, A. T. Weatherwax, and G. S. Bust (2013), GPS phase scintillation associated with optical auroral emissions: First statistical results from the geographic South Pole, *J. Geophys. Res. Space Physics*, *118*, 2490–2502, doi:10.1002/jgra.50214.

Kintner, P. M., B. M. Ledvina, and E. R. De Paula (2007), GPS and ionospheric scintillations, *Space Weather*, *5*, S09003, doi:10.1029/2006SW000260.

Knepp, D. L. (1983), Multiple phase-screen calculation of the temporal behavior of stochastic waves, *Proc. IEEE*, *71*(6), 722–737.

Prikryl, P., P. T. Jayachandran, S. C. Mushini, and R. Chadwick (2011), Climatology of GPS phase scintillation and HF radar backscatter for the high-latitude ionosphere under solar minimum conditions, *Ann. Geophys.*, *29*(2), 377–392.

Rino, C. L. (1979), A power law phase screen model for ionospheric scintillation: 1. Weak scatter, *Radio Sci.*, *14*, 1135–1145, doi:10.1029/RS014i006p01135.

Skone, S., and M. De Jong (2000), The impact of geomagnetic substorms on GPS receiver performance, *Earth Planets Space*, *52*(11), 1067–1071.

Skone, S., K. Knudsen, and M. De Jong (2001), Limitations in GPS receiver tracking performance under ionospheric scintillation conditions, *Phys. Chem. Earth Part A Solid Earth Geod.*, *26*(6), 613–621.

Skone, S., F. Man, F. Ghafoori, and R. Tiwari (2008), Investigation of scintillation characteristics for high latitude phenomena, in *Proceedings of the ION GNSS*, pp. 2425–2434, Inst. of Navigation, Savanna, Ga.

Smith, A. M., C. N. Mitchell, R. J. Watson, R. W. Meggs, P. M. Kintner, K. Kauristie, and F. Honary (2008), GPS scintillation in the high arctic associated with an auroral arc, *Space Weather*, *6*, S03D01, doi:10.1029/2007SW000349.

Van Dierendonck, A. J., J. Klobuchar, and Q. Hua (1993), Ionospheric scintillation monitoring using commercial single frequency C/A code receivers, in *Proceedings of the ION GPS*, vol. 93, pp. 1333–1342, Inst. of Navigation, Arlington, Va.

Yeh, K. C., and C. H. Liu (1982), Radio wave scintillations in the ionosphere, *Proc. IEEE*, *70*(4), 324–360.